

The Carbon Isotopic Ratio and Planet Formation

EDWIN A. BERGIN,¹ ARTHUR BOSMAN,¹ RICHARD TEAGUE,² JENNY CALAHAN,¹ KAREN WILLACY,³ L. ILSEDORE CLEEVEs,⁴
KAMBER SCHWARZ,⁵ KE ZHANG,⁶ AND SIMON BRUDERER⁷

¹*Department of Astronomy, University of Michigan, 1085 S. University Ave, Ann Arbor, MI 48109, USA*

²*Department of Earth, Atmospheric, and Planetary Sciences, Massachusetts Institute of Technology, Cambridge, MA 02139*

³*Jet Propulsion Laboratory, California Institute of Technology, 4800 Oak Grove Dr., Pasadena, CA 91109, USA*

⁴*Department of Astronomy, University of Virginia, Charlottesville, VA 22904*

⁵*Max Planck Institute for Astronomy, Königstuhl 17, Heidelberg, Germany*

⁶*Department of Astronomy, University of Wisconsin-Madison, 475 N. Charter St., Madison, WI 53706*

⁷*Max-Planck-Institut für Extraterrestrische Physik, Giessenbachstrasse 1, 85748 Garching, Germany*

(Accepted March 18, 2024)

Submitted to ApJ

ABSTRACT

We present the first detection of ¹³CCH in a protoplanetary disk (TW Hya). Using observations of C₂H we measure CCH/¹³CCH = 65±20 gas with a CO isotopic ratio of ¹²CO/¹³CO = 21±5 (Yoshida et al. 2022a). The TW Hya disk exhibits a gas phase C/O that exceeds unity and C₂H is the tracer of this excess carbon. We confirm that the TW Hya gaseous disk exhibits two separate carbon isotopic reservoirs as noted previously (Yoshida et al. 2022a). We explore two theoretical solutions for the development of this dichotomy. One model represents TW Hya today with a protoplanetary disk exposed to a cosmic ray ionization rate that is below interstellar as consistent with current estimates. We find that this model does not have sufficient ionization in cold (T < 40 K) layers to activate carbon isotopic fractionation. The second model investigates a younger TW Hya protostellar disk exposed to an interstellar cosmic ray ionization rate. We find that the younger model has sources of ionization deeper in a colder disk that generates two independent isotopic reservoirs. One reservoir is ¹²C-enriched carried by methane/hydrocarbon ices and the other is ¹³C-enriched carried by gaseous CO. The former potentially provides a source of methane/hydrocarbon ices to power the chemistry that generates the anomalously strong C₂H emission in this (and other) disk systems in later stages. The latter provides a source of gaseous ¹³C rich material to generate isotopic enrichments in forming giant planets as recently detected in the super-Jupiter TYC 8998-760-1 b by Zhang et al. (2021).

Keywords: editorials, notices — miscellaneous — catalogs — surveys

1. INTRODUCTION

The exoplanet revolution is now heading in a phase of greater characterization where the composition of planetary atmospheres can be explored in greater detail via high resolution spectroscopy (e.g., Line et al. 2021; Zhang et al. 2021; Brogi & Birkby 2021) or observations with new more sensitive instruments (e.g., JWST; JWST Transiting Exoplanet Community Early Release Science Team et al. 2023). A greater understanding of

composition allows for an exploration of how the formation conditions of the planet might be reflected in its composition. Over the past decade the strongest link has been to explore the bulk elemental abundance ratio of carbon to oxygen or C/O. Öberg et al. (2011b) first presented this idea utilizing basic chemistry (e.g., deposition/sublimation of primary molecular carriers of C and O) to show that the gas phase and solid-state C/O ratios are predicted to change with distance from the star and it might be possible to tie composition to the formation location. This may be more complicated as planets migrate, can accrete icy planetesimals/pebbles, and might have core-atmosphere mixing along with gravita-

tional settling (Cridland et al. 2016; Helled & Guillot 2017; Guillot et al. 2023). However, it captures a central element and is now widely compared to exoplanet atmospheric composition retrievals (Barman et al. 2015; Lavie et al. 2017; Oreshenko et al. 2017, to list a few).

Beyond the C/O ratio, the carbon isotopic ratio presents another interesting avenue for exploring the links between disk and exoplanet composition. This has been enabled by advances in high resolution spectroscopy of exoplanets that have isolated the $^{12}\text{C}/^{13}\text{C}$ ratio in two systems. In one case for a young, accreting super-Jupiter TYC 8998-760-1 b at 160 au, Zhang et al. (2021), measure a ratio of $^{12}\text{C}/^{13}\text{C} = 31_{-10}^{+17}$ (90% confidence). This is a significant ^{13}C enrichment when compared to the local interstellar value of 68 (Langer & Penzias 1993; Milam et al. 2005). A similar level of enrichment is found towards the Hot Jupiter WASP-77Ab, $^{12}\text{C}/^{13}\text{C} = 10.2\text{-}42.6$ at 68% confidence (Line et al. 2021). This enrichment is posited to have originated in molecular ices (Zhang et al. 2021). Curiously, the solar system betrays no evidence of ^{13}C enrichments at this level in any body, including comets that are comprised of molecular ices (Nomura et al. 2023). Further, interstellar ices towards quiescent lines of sight also show little evidence of enrichment (McClure et al. 2023). This points towards later phases, i.e., disk chemical evolution.

If molecular ices are enriched in ^{13}C within the disk, we should see some evidence of this in disk systems as the gas should exhibit the opposite (i.e., a depletion), provided the fractionation originates in the disk. The state-of-the-art of these measurements can be found in TW Hya, the nearest young gas-rich disk, and the best characterized system. Yoshida et al. (2022a) used the line wing emission of optically thick CO isotopologues to derive the carbon isotopic ratio in *gaseous* CO as a function of position. They find that ^{13}C isotopic enrichments are present in disk surface layers from $\sim 70\text{-}100$ au. The detection of $^{13}\text{C}^{18}\text{O}$ inside the CO snowline implies $^{12}\text{CO}/^{13}\text{CO} \sim 40_{-6}^{+9}$ in sublimated CO ices (Zhang et al. 2017). In contrast, the outer (>100 au) disk shows the opposite signature and appears to be depleted in ^{13}CO (Yoshida et al. 2022a).

However, the C/O ratio in TW Hya is measured to be > 1 (Bergin et al. 2016; Kama et al. 2016a). Thus, CO is not the only reservoir of carbon. Here we report the detection of weak ^{13}CCH emission within the TW Hya disk. The chemistry of CCH is the tracer of the excess carbon not carried by CO providing accurate measure of its isotopic ratio. To explore the origin of isotopic enhancements considering the full extent of isotopic measurements we use models of carbon fractionation of TW

Hya today (a later stage few Myr disk, i.e. class II) and in an early-stage (i.e. less evolved; class I) state. In §2 we will present our observations and the technique used to obtain the weak signal. §3 presents the derived isotopic ratio and the chemical models that are used to explore fractionation in the disk environment. Finally, in §4 we discuss the implications of this result and our conclusions.

2. OBSERVATIONS

2.1. C_2H

The C_2H data we use was originally published in Bergin et al. (2016) using the data from ALMA project 2013.1.00198.S. We refer the reader to the original article for details on the data reduction and imaging. This included the subtraction of the continuum by modeling the continuum contribution as a linear component around the line emission and using the `uvcontsub` task to remove this in the image plane. Note that as the continuum emission is confined to inside of $\sim 1''$ (~ 60 au), the continuum subtraction should have minimal effect on the line data presented here. The resulting images have a beam of $0.50'' \times 0.41''$ with a position angle of 59.0° .

Figure 1 shows the integrated flux density for the $N = 4 - 3$ $J = 9/2 - 7/2$ $F = 5 - 4$ transition made using a Keplerian mask assuming $i = 6.8^\circ$, $\text{PA} = 151^\circ$, $M_{\text{star}} = 0.6 M_{\text{sun}}$ and $d = 60.1$ pc. The mask was used rather than σ -clipping to remove any contribution from the $F = 4 - 3$ transition. The radial profile is well described by a Gaussian centered at $1.1''$ with a width of $0.58''$ (Bergin et al. 2016).

Integrating over the whole disk yields a total integrated flux of 6.17 ± 1.16 Jy kms^{-1} where the uncertainties have been calculated following Teague et al. (2019), while over the annulus with an inner radius of $0.52''$ (31 au) and an out radius of $1.68''$ (101 au) we find 4.20 ± 0.68 Jy km s^{-1} . The peak intensity was 372 ± 6 mJy beam^{-1} .¹

The non-Gaussian beam which results from the imaging process can introduce subtle inaccuracies when calculated integrated fluxes. Following Czekala et al. (2021), the non-Gaussianity of the beam can be quantified with ϵ , which is the ratio of the volumes of the CLEAN and dirty beams, where $\epsilon = 1$ indicates a purely Gaussian beam. Using the scripts released as part of the MAPS Large Program (Öberg et al. 2021) to ap-

¹ There is a difference in this intensity and that given in Table 1 of Bergin et al. (2016) where the peak intensity for this transition is listed as 1.100 ± 0.007 Jy beam^{-1} . In this work we deblended the $F = 5-4$ and $4-3$ which was not done by Bergin et al. (2016).

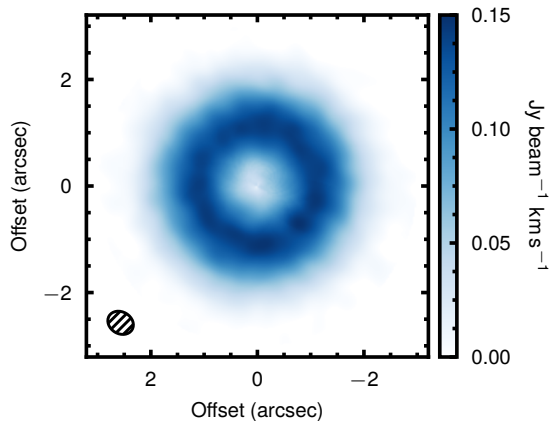


Figure 1. Zeroth moment of the $N = 4 - 3$ $J = 9/2 - 7/2$ $F = 5 - 4$ transition of C_2H made using a Keplerian mask. The peak value is $148.7 \text{ mJy beam}^{-1} \text{ km s}^{-1}$. The beam size is shown in the bottom left of the panel.

ply a correction to this (the so-called ‘JvM correction’), the C_2H data were found to have $\epsilon = 0.69$. Calculating the integrated flux density and peak intensity with the JvM-corrected data found discrepancies of 5% and 2%, respectively. These uncertainties were incorporated in the ratios described below by adding this uncertainty in quadrature to the statistical uncertainty.

2.2. ^{13}CCH

The ^{13}CCH line observations of TW Hya were carried out by ALMA on November 23, 2016 (2015.1.00308.S). The array included 42 antennas, with baselines lengths spanning from 15 to 704 m. The correlators were set to have three-line windows centered on 336.571, 351.060, and 349.346 GHz, and each window had a bandwidth of 467 MHz. A fourth spectral window was dedicated to continuum observations, centering on 338.769 GHz with a band width of 2 GHz. The Nearby Quasars J1037-2934, J1058+0133, J1107+4449 were used for gain, bandpass, and flux calibration, respectively. The total on-source time was 49 minutes. The raw visibility data were calibrated by NRAO staff members in CASA version 4.7.0, and we further applied phase-only self-calibration on the data using the continuum spectral window and line-free channels in all three-line spectral windows. The fully calibrated visibilities were then Fourier inverted to generate images by using the CLEAN task with a Briggs weight of 0.5. The final ^{13}CCH image has a noise level of $3.6 \text{ mJy beam}^{-1}$ per 210 ms^{-1} channel and a beam size of $0.32'' \times 0.30''$ with a position angle of 4.4° .

To extract a disk-averaged spectrum we use the Python package *GoFish* (Teague 2019) which implements the method presented in Yen et al. (2016).

First the spectrum in each pixel was shifted to the systemic velocity by applying a shift of $\delta v(r, \phi) = -v_{\text{kep}}(r) \cos \phi \sin i$, where $v_{\text{kep}}(r)$ is the Keplerian rotation at radius r , ϕ is the polar angle of the pixel, measured relative to the red-shifted major-axis, and i is the disk inclination. With all spectra centered on the systemic velocity, they are stacked to increase the signal-to-noise of the spectrum. This method will result in the average spectrum in a pixel within the averaged area. To obtain an integrated flux density, this average spectrum is scaled by the total area of the annulus over which the spectra were averaged. This approach of first averaging and then scaling is mathematically the same as integrated over the entire area, however the intermediate averaged spectrum allows for a more accurate determination of the integration boundaries.

For the velocity shifting we assume the same parameters as for the Keplerian mask in the previous section, $i = 6.8^\circ$, $\text{PA} = 151^\circ$, $M_{\text{star}} = 0.6 M_{\text{sun}}$ and $d = 60.1 \text{ pc}$. Assuming that the radial emission profile of ^{13}CCH follows that of C_2H , we average from $0.52''$ (31 au) to $1.68''$ (101 au) to increase the signal-to-noise ratio of the detection, weighting each individual annulus by their respective area. As each annulus has a fixed width of $1/4$ of the beam FWHM ($\sim 80 \text{ mas}$), the weights are simply proportional to r^2 .

To verify that the image was centered, we vary the source center by small pixel-scale offsets and measure the signal-to-noise ratio of spectrum. We find a peak signal-to-noise with an offset of $(\delta x_0, \delta y_0) = (-52 \text{ mas}, -155 \text{ mas})$.

The resulting spectrum is shown in Fig. 2, showing the clear detection of the $F_2 = 11/2 - 9/2$ and $F_2 = 9/2 - 7/2$ components of the $N = 4 - 3$, $J = 9/2 - 7/2$ $F_1 = 5 - 4$ transition. Integrating this spectrum yields an integrated flux of $56.9 \pm 14.1 \text{ mJy km s}^{-1}$. We have verified by changing the inner and outer radii of the annuli we integrate over that this range gives the highest signal-to-noise detection of the lines. Integrating over the whole disk finds an integrated flux of $70.2 \pm 23.2 \text{ mJy km s}^{-1}$. From Gaussian fits to the line, the peak intensity values for the bright annulus region were $0.9 \pm 0.3 \text{ mJy beam}^{-1}$ and $1.2 \pm 0.3 \text{ mJy beam}^{-1}$ for the $F_2 = 11/2 - 9/2$ and $F_2 = 9/2 - 7/2$ components, respectively.

To verify that the non-Gaussianity of the beam did not bias the results, the JvM-correction (Czekala et al. 2021) was applied to the ^{13}CCH data. These data were found to have $\epsilon = 0.70$, consistent with the C_2H data, which is unsurprising given they use the same antenna configuration. The integrated flux density was not found to substantially vary compared to the native data, finding only a 1% difference. The peak intensity varied more, up

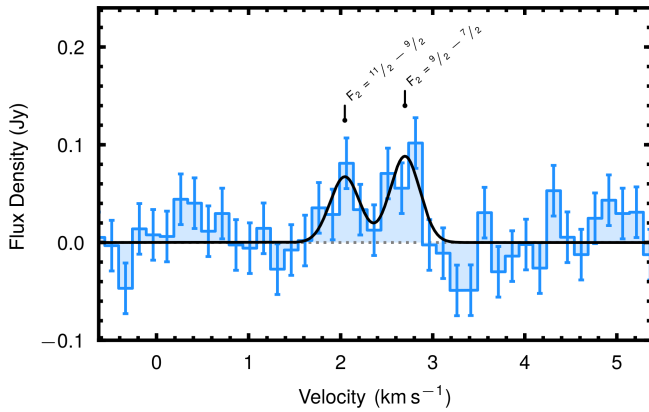


Figure 2. Integrated average flux density between $0.8''$ and $1.8''$, resampled to a velocity resolution of 150 m s^{-1} , clearly showing the $F = 11/2 - 9/2$ and $F = 9/2 - 7/2$ components of the $N = 4 - 3$, $J = 9/2 - 7/2$ transition. The black lines show two Gaussian fits to the spectrum with a shared line width of 125 m s^{-1} .

to 40%, however this is because such a low-level signal is dominated by the noise which is substantially suppressed with the JvM-correction. As such, this term is ignored as the difference is equivalent to the difference in the noise levels determined by the RMS of a line-free channel. The 1% uncertainty on the integrated flux density is added in quadrature to the statistical uncertainties.

3. CARBON ISOTOPIC RATIO IN TW HYA

3.1. $^{12}\text{C}^{12}\text{H}/^{13}\text{C}^{12}\text{H}$ in TW Hya

Using the integrated intensities from above, we find a $\text{C}_2\text{H} / ^{13}\text{CCH}$ ratio of 74 ± 22 in the bright annulus and 88 ± 34 averaged over the whole disk. Similarly, if we use the peak flux density for each line, after correcting for the relative beam sizes and assuming that they’re optically thin so that the two F_2 components can be added, we find a $\text{C}_2\text{H} / ^{13}\text{CCH}$ ratio of 78 ± 15 , consistent with the integrated flux approach. The above ratios are ratios in flux and not total column. Based on the fact that the flux ratio is consistent with the interstellar $^{12}\text{C}/^{13}\text{C}$ isotopic ratio (~ 68 Langer & Penzias 1993; Milam et al. 2005) and hyperfine ratios (Bergin et al. 2016), the C_2H emission in TW Hya is optically thin. In this limit, for observations that have been corrected for differences in the beam size (as above), the integrated flux density ratio is essentially equivalent to the overall column density ratio correcting for an 11% difference in the A-coefficients. We therefore conclude that $N(\text{CCH})/N(^{13}\text{CCH}) = 65 \pm 20$ over spatial scales commensurate with the TW Hya C_2H ring.

3.2. Two Carbon Isotope Reservoirs

Fig. 3 provides the landscape of isotopic ratio measurements within TW Hya, with explicit values given in Table 1. Inside of the CO snowline at 21 au (Schwarz et al. 2016) an isotopic ratio of $\sim 40_{-6}^{+9}$ is measured via detection of $^{13}\text{C}^{18}\text{O}$ by Zhang et al. (2017). Hily-Blant et al. (2019) observe HCN and H^{13}CN and measure an average ratio of 86 ± 4 inside 60 au. The differences between CO, HCN, and CN provide evidence of multiple isotopic reservoirs in the system as noted by Hily-Blant et al. (2019) and Yoshida et al. (2024). This is further traced when comparing the $^{12}\text{C}/^{13}\text{C}$ as estimated for CO and CCH. In TW Hya CCH emits in a ring at radii of ~ 40 -110 au (Fig. 1; Bergin et al. 2016) and our detection of ^{13}CCH must arise from within the ring where we measure a ratio of $^{12}\text{C}/^{13}\text{C}$ in CCH of 65 ± 15 . In contrast, over a similar spatial extent, Yoshida et al. (2022a) estimate a $^{12}\text{C}/^{13}\text{C}$ ratio of 21 ± 5 in CO. If the isotopic ratio of 21 existed in CCH in our data then we would have a 14σ detection ^{13}CCH in the integrated emission, which is in contrast to the current 4σ detection. This re-enforces the evidence that there are two isotopic reservoirs for carbon present in TW Hya as argued previously by Yoshida et al. (2022a) for carbon. We note two isotopic reservoirs have also been isolated for nitrogen by Hily-Blant et al. (2019).

4. MODEL OF DISK CARBON ISOTOPIC CHEMISTRY

To examine the origins of two isotopic reservoirs for carbon in the TW Hya disk we use a detailed model of the carbon isotopic chemistry for TW Hya. For this purpose, we use the Dust And Lines thermochemical model (DALI) code (Bruderer et al. 2012; Bruderer 2013). Our aim is to explore a generic model of the chemistry of carbon isotopic fractionation in two frameworks. One is an extant model of the TW Hya disk that has been used in previous modeling efforts (Trapman et al. 2017; Bosman & Banzatti 2019). We call this model the “late-stage disk” model as it is motivated by the TW Hya Class II disk as it is today with numerous observational constraints. In addition, we present an “early-stage” model that explores the origins of isotopic chemistry during earlier phases more consistent with a Class I disk. In our efforts we will not fit the overall emission levels; rather, we will explore whether two separate carbon isotopic reservoirs are created. That is, we are not attempting to fully match this system but rather attempting to explore the conditions that may lead to carbon isotopic fractionation.

We use the extant TW Hya model published by Trapman et al. (2017) and Bosman & Banzatti (2019). The

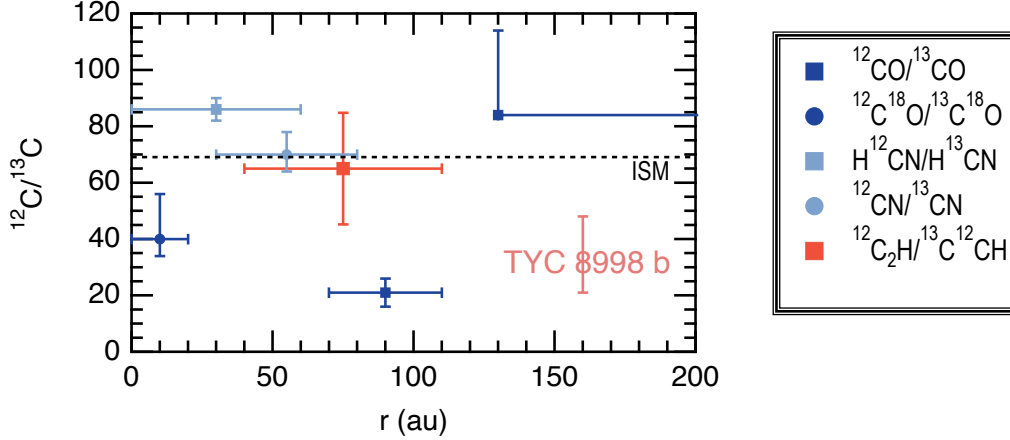


Figure 3. Measurements of isotopic ratios in TW Hya placed into observational context in terms of distance from the star. Measurements are from Yoshida et al. (2022a, CO), Zhang et al. (2017, C^{18}O), Hily-Blant et al. (2019, HCN), and CCH (presented here). For illustrative purposes, we also include the measurement of TYC 8998 b (Zhang et al. 2021) which is shown at the orbital distance estimated from its host star.

Table 1. $^{12}\text{C}/^{13}\text{C}$ in TW Hya

Location (au)	Molecular Carrier	$^{12}\text{C}/^{13}\text{C}$ Ratio	Reference
0 – 20	$^{12}\text{C}^{18}\text{O}/^{13}\text{C}^{18}\text{O}$	40^{+9}_{-6}	Zhang et al. (2017)
< 60	$\text{H}^{12}\text{CN}/\text{H}^{13}\text{CN}$	86^{+4}_{-4}	Hily-Blant et al. (2019)
25 – 55	$^{12}\text{CN}/^{13}\text{CN}$	70^{+8}_{-6}	Yoshida et al. (2024)
70 – 110	$^{12}\text{CO}/^{13}\text{CO}$	21^{+5}_{-5}	Yoshida et al. (2022a)
40 – 110	$^{12}\text{CCH}/^{13}\text{CCH}$	65^{+20}_{-20}	This Paper
> 130	$^{12}\text{CO}/^{13}\text{CO}$	> 84	Yoshida et al. (2022a)

basic parameters of the model are given in the appendix. The chemical network including isotopic fractionation is created by Miotello et al. (2014) and includes key fractionation reactions linking ^{12}C and ^{13}C (Langer et al. 1984; Röllig & Ossenkopf 2013). The critical reactions in this case are the primary fractionation reaction:



which favors ^{13}CO at low ($\lesssim 40$ K) temperature. The other key isotopic fractionation pathway in the disk is isotopic selective photodissociation of CO and we use the rate prescription of Visser et al. (2009). For a basic introduction to carbon isotopic fractionation in the disk framework we refer the reader to Woods & Willacy (2009) and to the review by Nomura et al. (2023). In this model we include a grain surface chemistry that is limited to simple hydrogenation reactions to make saturated species (e.g. water, ammonia, methane). Further, the overall network does not extend to methanol.

4.1. Late-Stage Model

Here, we use the existing model of TW Hya by Trapman et al. (2017) and Bosman & Banzatti (2019). This model has been designed to match several well characterized aspects of this disk. First, the strong mm-continuum image and scattered light surface requires grain growth and settling (van Boekel et al. 2017). Further, the mm-continuum emission shows that the large grains are more spatially confined compared to the gas (Andrews et al. 2016; Huang et al. 2018). We therefore, assume the disk is several Myr-old (Sokal et al. 2018) with 99% of the grain mass confined to the midplane to match the mm-wave dust emission distribution.

The primary ionization sources towards this disk (ultraviolet, X-ray, cosmic rays) have been constrained via observations. For thoroughness the UV field is the stellar spectrum of TW Hya with UV excess from Cleeves et al. (2015). We adopt $L_X = 1.4 \times 10^{30} \text{ ergs s}^{-1}$ with a plasma temperature of 3 MK (Stelzer & Schmitt 2004).

Table 2. Initial Chemical Abundances^a

Species	Late Stage	Early Stage
H ₂	0.5	0.5
He	7.6×10^{-2}	7.6×10^{-2}
Mg	4.2×10^{-10}	4.2×10^{-10}
Si	7.9×10^{-9}	7.9×10^{-9}
S	1.9×10^{-9}	1.9×10^{-9}
Fe	4.3×10^{-10}	4.3×10^{-10}
CH ₄	2.7×10^{-6}	...
¹³ CH ₄	3.5×10^{-8}	...
CO	2.7×10^{-6}	2.7×10^{-4}
¹³ CO	3.5×10^{-8}	3.5×10^{-6}
N ₂	1.1×10^{-5}	1.1×10^{-5}
N ¹⁵ N	2.4×10^{-8}	2.4×10^{-8}
H ₂ O _{ice}	2.6×10^{-6}	2.6×10^{-6}

^aRelative to H

The cosmic ray ionization rate (ζ_{cr}) is assumed to be 10^{-19} s^{-1} which is constrained via chemical analysis of molecular ion emission (Cleeves et al. 2015). Additional information is found in the original reference for this model (Trapman et al. 2017).

Analysis of numerous disk CO isotopologue observations, starting with TW Hya (Favre et al. 2013), have found that the abundance of CO appears to be reduced in disk gas (see discussion in Miotello et al. 2023). Essentially, CO is believed to be provided to the disk with an “interstellar” abundance relative to H₂ $\sim 10^{-4}$ (Bergin & Williams 2017). Some regions of the disk have temperatures below the CO sublimation temperature (~ 20 K) and CO ice forms. However, in regions where the dust temperature is > 20 K, the expectation is that the CO gaseous abundance will be interstellar. However, in systems where strong constraints on the H₂ mass exist, such as TW Hya, the CO gas phase abundance is found to be depleted, i.e. $[\text{C}/\text{H}]_{\text{gas}} < [\text{C}/\text{H}]_{\star}$ (Favre et al. 2013; Kama et al. 2016b; Zhang et al. 2017, 2019). This has now been confirmed via a direct measurement of the H₂ density through pressure broadened line wings (Yoshida et al. 2022b). The depletion of CO (and also water vapor; Du et al. 2017) is believed to occur via chemical processing of CO into species with lower volatility, such as CO₂ or CH₃OH, and via interactions with grain evolution (see Krijt et al. 2020, for comprehensive model). In sum, the Trapman et al. (2017) model assumes that overall gas-phase carbon is depleted relative to ISM levels, with the missing carbon present as ices on the mm-grains that are settled to the midplane and more spatially confined than the gas.

Finally, we assume C/O ~ 2 based on the analysis from C₂H (Bergin et al. 2016; Kama et al. 2016a). This model

assumes that 50% of the remaining gaseous carbon is in CO and 50% originally in CH₄. The presence of the CH₄ has been previously shown to generate strong C₂H emission in disks (Bosman et al. 2021a).² Our model is run for 1 Myr, which is much less than the estimated age of TW Hya (~ 8 Myr; Sokal et al. 2018). This difference is because we are not modeling the CO abundance evolution, which we assume took place during earlier stages. Rather our goal is to explore whether existing TW Hya chemical models can readily fractionate carbon carriers to create two interdependent and stable isotopic reservoirs. Table 2 provides the overall initial chemical abundances.

With this calibrated model we explored whether this physical perspective could produce two separate isotopic reservoirs. For this purpose, we include a network that includes fractionation of carbon (Miotello et al. 2014). The results are shown in Fig. 4. In this Figure, panel (a) provides the vertical density and thermal profile. In panels (b-d) we show model predictions as a vertical cut taken at 63 au. This location traces the C₂H ring and is commensurate with where C₂H and CO appear to trace two separate isotopic reservoirs (Fig. 3). The figure shows the C₂H, CO, and CH₄ vertical distributions in abundance alongside the ¹³C isotopologues. In our models the initial isotopic ratio in both CO and CH₄ is 77 and we seek to determine if the overall isotopic chemistry produces two separate reservoirs. The full chemical evolution from this model with the major carriers shown is given in Fig. 5.

Exploring panel (b) in Fig. 4 we find an interesting fractionation pattern for CO. At the upper surface, near $z = 25$ au, the effects of CO isotopic selective photodissociation are found with a deficit in ¹³CO. Deeper in the disk there is a dip in the ¹³CO abundance near $z = 17$ au that produces a sharp increase in ¹²CO/¹³CO over a short vertical distance. The gaseous CO isotopic ratio estimated from column density ratios at 63 au is 79 which is well above the observed value of 21.

In layers above the midplane ($4 \text{ au} < z < 20 \text{ au}$) where CH₄ ice sublimates, much of the excess carbon provided by CH₄ is processed into hydrocarbon ices (C₂H₂ and HCCH₂; Fig. 5). Above the edge of this vertical zone near 20 au gaseous C₂H production peaks. For C₂H, the model predicts a complex fractionation pattern. However, it is important to focus on vertical layers where C₂H is found in abundance between $14 \text{ au} < z < 24 \text{ au}$. Here, some of the excess carbon resulting from isotopic

² Specifically this paper states that the origin of C₂H arises from CH₄ released from carbon in refractory organics. However, this is simulated in the system by putting carbon in CH₄.

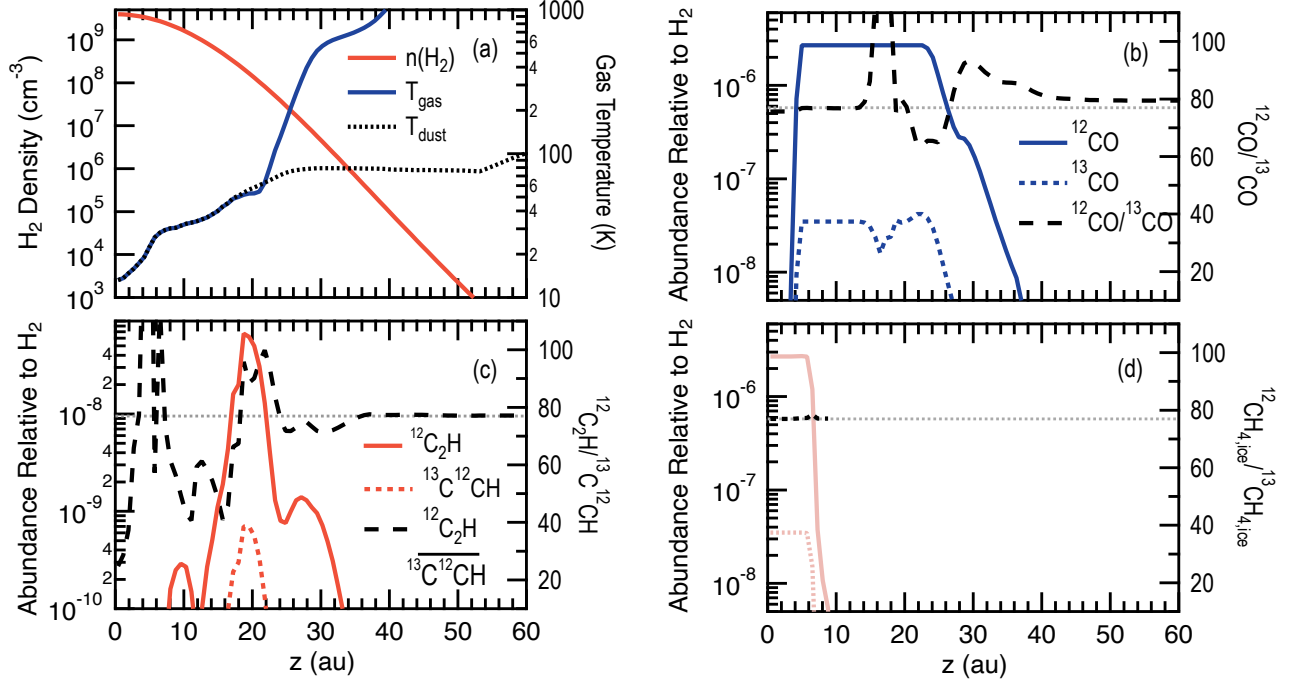


Figure 4. Predicted vertical distribution of CO, CCH, and CH₄ ice isotopic ratios in the “late-stage disk” model at a radial location commensurate with the center of the C₂H emission ring (63 au). (a) Overall gas density structure and modeled vertical gas thermal profile at this radius. (b,c,d) Predicted vertical distribution of CO/¹³CO, C₂H/¹³CCH, and CH_{4,ice}/¹³CH_{4,ice} from the thermochemical model. In these panels the chemical abundances are referenced to the left axis while the dashed line provides the predicted isotopic ratio that is referenced to the axis on the right. For all species the initial isotopic ratio is 77 which is shown as the dotted grey line.

selective photodissociation of CO finds its way into C₂H raising the ¹³CCH abundance above the initial value, with a sharp decrease in CCH/¹³CCH at $z = 18$ au as the ¹³C finds its way into hydrocarbon ices. The gaseous C₂H isotopic ratio estimated from column density ratios is 78 which agrees with observations (Table 1). The predicted total C₂H column density at this radius is 6×10^{14} cm⁻². This would give an integrated flux density for the N=4-3 J=9/2-7/2 F-5-4 transition of ~ 0.2 Jy km/s in a 0.45'' beam at 60 pc (assuming a gas temperature of 40 K). This is close to the observed peak integrated flux density within the emission ring (see Fig. 1). We also confirm that the gas phase C/O ratio in the model is 2 in the C₂H emitting layer, which is consistent with previous work (Bergin et al. 2016).

In summary, there is a narrow range of physical parameters where ¹³C fractionation is found, which limits the impact over the entire column. This particular “late-stage disk” model is incapable of producing two separate isotopic ratios for CO and C₂H (and HCN). As a final check, to explore whether the excess CH₄ in the gas could hide the presence of isotopic fractionation, we ran an identical model with no excess CH₄ as an initial

condition. This model did not produce significant carbon isotopic fractionation of CO or C₂H. For this set of initial conditions, the C/O ratio is effectively solar at these distances (i.e. C/O = 1) and, as a result, the C₂H column was reduced by 3 orders of magnitude. This is consistent with earlier analyses (Bergin et al. 2016; Cleves et al. 2018; Bosman et al. 2021b).

4.2. Early-Stage Disk Model

4.2.1. Motivation

Our model of TW Hya as it exists today is incapable of producing two separate carbon isotopic reservoirs. We therefore also explore a model of a younger disk where conditions might be significantly different. Our hypothesis is as follows. Numerous works have shown that, if cosmic rays are present, CO can be chemically processed into a variety of less volatile species which may relate to the reduced abundance of CO as seen in numerous disk systems (Bergin et al. 2014; Furuya & Aikawa 2014; Reboussin et al. 2015; Eistrup et al. 2017; Schwarz et al. 2018; Bosman et al. 2018). Perhaps this process might also lead to isotopic fractionation of CO and thereby simultaneously set the stage where another

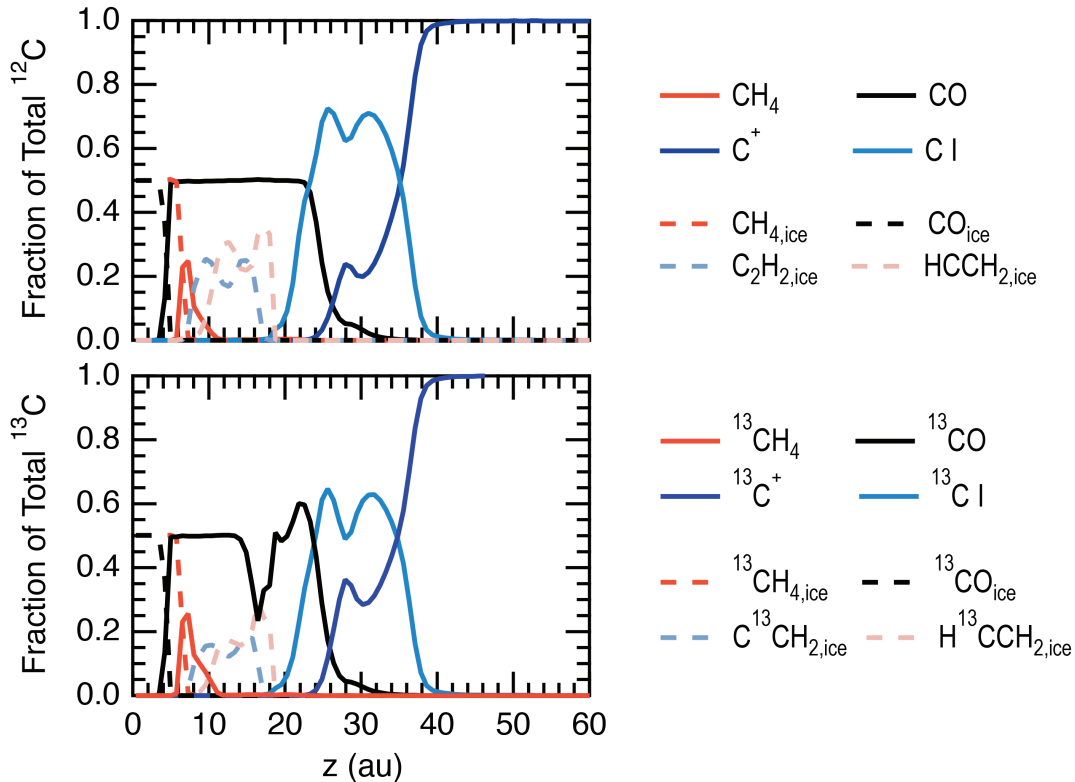


Figure 5. Plot of (top) major carriers of ^{12}C and (bottom) ^{13}C . Abundances are normalized to the total amount of isotopic carbon with $x(^{12}\text{C}) = 5.2 \times 10^{-6}$ and $x(^{13}\text{C}) = 7.0 \times 10^{-8}$ (abundances given relative to total H). This model is sampled at $r=63$ au, the location of the C_2H emission ring. We note that $\text{HC}^{13}\text{CH}_2$ is not shown here but has the same distribution and abundance as $\text{H}^{13}\text{CCH}_2$.

carbon-bearing molecule would carry the opposite isotopic signature. If this carbon-bearing molecule were a hydrocarbon then it might provide the excess carbon needed to generate strong C_2H emission at later stages.

The chemical processing of CO appears to be time dependent as two independent analyses of C^{18}O and lesser abundant isotopologues find a decline in the gaseous CO abundance from the initial interstellar level as a function of evolutionary state corresponding to ~ 1 Myr timescales (Bergner et al. 2020; Zhang et al. 2020). Along these lines the gaseous C/O ratio might also change as the disk evolves. Interstellar ices have some CO and CH_4 (Öberg et al. 2011a). These ices would sublimate at 30 K (Minissale et al. 2022) to mix with CO gas that has $\text{C/O} = 1$. However, interstellar CH_4 ice is only $\sim 10\%$ of the CO ice content (McClure et al. 2023). When both sublimate to the gas at 30-40 K (with water and CO_2 frozen), the resulting composition is effectively $\text{C/O} \sim 1$. Given that observational analyses are suggesting that TW Hya has $\text{C/O} \sim 1.5-2$ there also must be some additional chemical evolution in the volatile inventory and its C/O ratio.

In this light, cosmic rays are known to be present in well characterized pre-stellar cores with measured ionization rates consistent with expectations for the dense interstellar medium (Maret & Bergin 2007; Redaelli et al. 2021). In contrast, Class II systems appear to have reduced ionization that are argued to be the result of cosmic ray exclusion by magnetized winds (analogous to the solar system’s heliosphere) or tangled magnetic fields within the disk environment (Cleeves et al. 2015; Aikawa et al. 2021; Seifert et al. 2021). Class I systems still have residual envelopes that limit the reach of magnetized stellar winds, restricting their effect to the extent of the cavity carved by the protostar’s energetic flows (Arce et al. 2007; Hsieh et al. 2023). Within the outflow cavity it is possible that cosmic rays are excluded. However, energetic particles might still penetrate through envelope and into the protostellar disk through equatorial zones. Overall, it is possible that changes in the ionization rate are associated with the clearing of the envelope from the protostellar to the protoplanetary disk stage. It has long been recognized that cosmic ray ionization is central towards the isotopic fractionation of carbon in the interstellar medium (Langer et al. 1984;

Langer & Graedel 1989; Furuya et al. 2011; Roueff et al. 2015). Perhaps ionization evolution might also provide some imprint on isotopic ratios carried through subsequent evolutionary stages.

4.2.2. Model and Results

To model an earlier stage TW Hya *protostellar* disk (e.g., Class 0/I), we assume the grains have grown but only 90% of their mass is in large grains (i.e., mm-sized). We also include the presence of cosmic rays ($\zeta_{\text{H}_2} = 5 \times 10^{-17} \text{ s}^{-1}$). This value is at a level a factor of 50 above that currently estimated towards TW Hya by Cleeves et al. (2015) which was used in the late-stage disk simulation. The initial chemical abundances, given in Table 2, place the initial CO abundance at 2.7×10^{-4} (i.e. interstellar) with no additional carbon in any form. Thus, we assume that there has been no chemical processing of CO as assumed in the earlier model. The initial CO isotopic ratio is also set to an interstellar isotopic ratio of 77. At the start of the simulation the only reservoir of ^{12}C and ^{13}C is CO. This model has some water ice included with an abundance 2.7×10^{-6} and is run for 1 Myr. Here we assume that a significant amount of water ice has accumulated in the midplane where most of the dust mass still resides (Krijt et al. 2016). The baseline model structure parameters are given in the appendix.

Fig. 6 presents the results from this model at $r = 63$ au in the form of vertical cuts of the abundance distribution of key isotope carriers. Fig. 7 provides the overall carbon inventory over this same region. Comparison of the thermal structure between the late-stage (Fig. 4) and early-stage (Fig. 6) disk model show that the less evolved system, with a larger mass in small grains, traps radiation higher in the disk leading towards slightly cooler deeper layers. Further the gas phase abundance of CO is distributed within the warm molecular layer (i.e., above the CO freeze-out layer in the midplane and below the photodissociation layer; Aikawa et al. 2002) which exists over a wider range in vertical distance (Fig. 6b). As in the late-stage disk model (Fig. 4), C_2H forms at intermediate heights albeit in slightly higher layers in the early-stage disk model shown in panel (c) in Fig. 6. One additional difference for C_2H is the peak abundance of C_2H is reduced by about an order of magnitude as the amount of free carbon is reduced in this model. The total C_2H column density from this model (at $r = 63$ au) is $5 \times 10^{12} \text{ cm}^{-2}$. This is two orders of magnitude reduced from the late-stage model. In this model the C/O ratio in the gas is near unity and a reduction in the C_2H column/line flux density is expected.

In the early-stage disk model at high altitude ($z=35$ au; Fig. 6b) CO is destroyed via photodissociation. Within the layer where CO is photodestroyed the effects of isotopic selective photodissociation of CO are observed and $^{12}\text{CO}/^{13}\text{CO}$ exceeds the assumed initial value shown as the dotted line. More substantive changes are seen deep within the warm molecular layer where cosmic rays chemically process about 40% of gas phase CO into methane ice (Fig. 6b and c). The chemical processing of CO is initiated via reactions with He^+ atoms which free $^{12}\text{C}^+$ and $^{13}\text{C}^+$ alongside O atoms (Aikawa et al. 1996). The oxygen atoms collide with cold dust grains and hydrogenate to form water ice. In this model about 40% of the O in CO is placed into water ice leaving excess C^+ in the gas. This causes the drop in the CO abundance near $z = 14$ au Fig. 6b).

This excess ionized carbon would normally find its way to CO, but the lack of oxygen means it sits in a sea of H_2 gas. As noted by Du et al. (2015) this leads to the formation of unsaturated and saturated hydrocarbons that work towards species that can freeze onto grains when their individual sublimation temperature is above the temperature of the dust. In this instance the *gas-phase* chemistry favors the formation of mostly CH_4 ice but also C_2H_2 and HC_2H_2 ices.

In the layer where gas phase CO chemical processing occurs, cosmic rays are also powering carbon isotopic fractionation. In this case, the He^+ destruction of CO and ^{13}CO produces an excess $^{13}\text{C}^+$ atoms which are favored to be implanted into ^{13}CO via reaction (1) due to the low gas temperature in these layers ($T_{\text{gas}} < 40$ K). In all, ^{13}CO gas becomes modestly enriched with $^{12}\text{C}/^{13}\text{C} \sim 50$ compared to the initial value of 77. Because the ^{13}C becomes locked in gaseous CO, the hydrocarbon ices carriers have $^{12}\text{C}/^{13}\text{C} > (^{12}\text{C}/^{13}\text{C})_{\text{ISM}}$.

Similar behavior is seen throughout the disk, but at variable height about the midplane. In Fig. 8 we provide the $^{12}\text{C}/^{13}\text{C}$ ratio in CO and methane ice as a function of radius. For this plot we have computed the ratio from the estimated vertical column densities. This demonstrates that this model effectively produces two isotopic reservoirs for carbon across much of the disk. In the bottom panel of the Figure, we also provide the column densities of the main isotopologues. The comparable column density between gaseous CO and CH_4 ice shows that this effect is present both radially and vertically. We note that the midplane ($z < 3$ au) remains unchanged by this evolution with CO ice as the dominant carbon carrier for both isotopologues and the ratio fixed at 77.

One issue that we have not addressed is fact that the CO isotopic ratio appears to be elevated above ISM val-

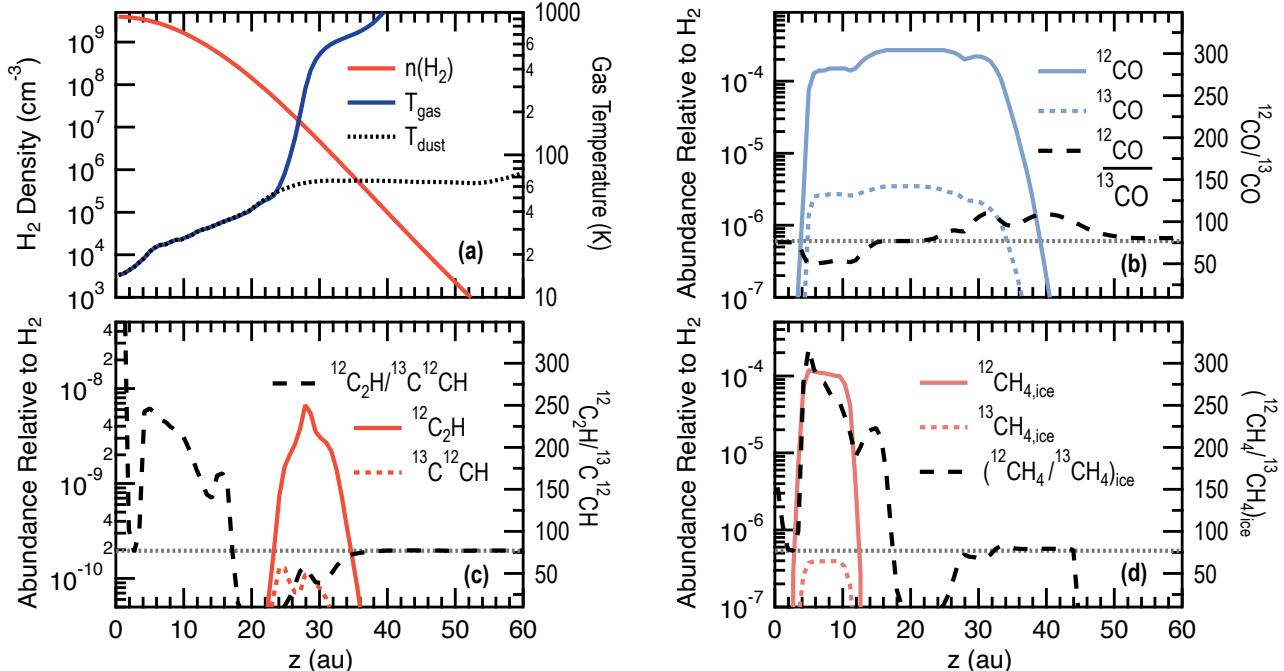


Figure 6. Predicted vertical distribution of CO and CCH isotopic ratios in the “early-stage disk” model at a radial location commensurate with the center of the C₂H emission ring (63 au). (a) Overall gas density structure and modeled vertical gas thermal profile at this radius. (b), (c), (d) Predicted vertical distribution of ¹²CO/¹³CO, ¹²C₂H/¹³C¹²CH, and ¹²CH₄/¹³CH₄ from the thermochemical model. In these three panels the chemical abundances are referenced to the left axis while the dashed line provides the predicted isotopic ratio that is referenced to the axis on the right. In this model all ¹³C is placed in CO at the start with an initial isotopic ratio of 77, which is shown as the dotted grey line. This model is sampled at r=63 au, the location of the C₂H emission ring.

ues beyond 130 au (see Fig. 3). Earlier work by Zhang et al. (2019) inferred extreme CO depletion values beyond 100 au (i.e., abundances reduced by factors of 100 more compared to interstellar levels). They suggested that this may be the result of gaseous dissipation of the disk. If this is the case, then the elevated CO isotopic ratio at these large distances could be the result of isotopic selective photodissociation. If this is the case, then perhaps isotopic ratios might be used as a probe of gas disk dissipation.

4.2.3. Critical Dependencies

We have made a number of assumptions in this model including the presence of cosmic rays, increasing the amount of small grains, and reducing the amount of water ice present in upper layers. Of these we find that the first two are important for the generation of the isotopic enrichments. Cosmic ray ionization has the highest penetration power, and if present, clearly will dominate the ion-molecule chemistry leading to fractionation. However, high levels of hard X-rays (> 1 keV), with scattering, might also be important (Igea & Glassgold 1999). Increasing the ratio of small to large grains (i.e. more mass in small grains) leads to a more flared surface and

a higher mass present below 35 K (e.g. compare Figs 4a and Fig. 6a). In this model this effect is not large (~20% more mass below 35 K in the early-stage model), but can be expected to be higher with less dust evolution and higher flaring angles. Another aspect is the greater amount of small grains increases the effective surface area ($\langle n\sigma \rangle_{gr}$) of grains, enhancing the dust/gas interaction and enabling greater freeze-out of methane. For the last factor, the assumed water ice abundance, we find that if we assume an initial water ice abundance in the early-stage model of 10^{-4} (relative to H) as opposed to the original value of 2.6×10^{-6} then there is no major difference in the overall chemistry compared to the results presented in Figs. 6 and 7. While fractionation levels and abundances of key carriers (CO, CH₄) are unaffected, the C₂H column is altered and is reduced by an order of magnitude.

5. DISCUSSION

For the past decade observational analyses of resolved gas-rich disks have revealed two puzzles. One regards the overall abundance of CO which appears to be below the expected value of 10^{-4} relative to H₂ (Favre

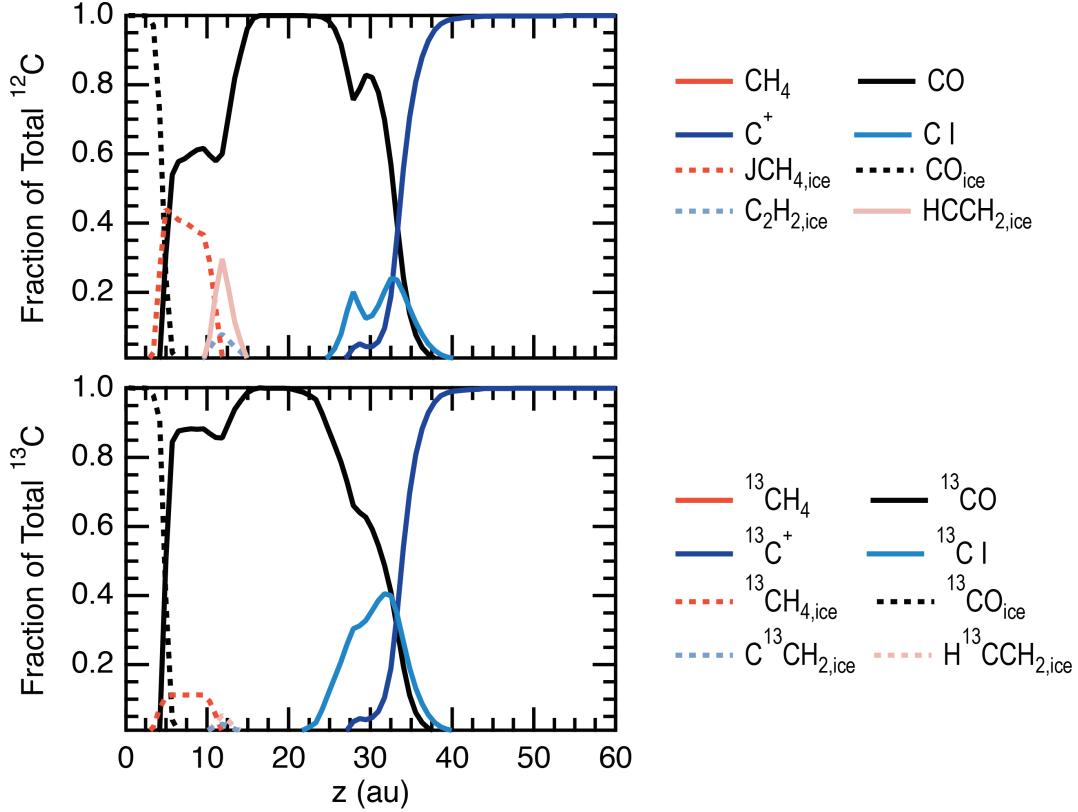


Figure 7. Plot of (top) major carriers of ^{12}C and (bottom) ^{13}C . Abundances are normalized to the total amount of isotopic carbon with $x(^{12}\text{C}) = 2.7 \times 10^{-4}$ and $x(^{13}\text{C}) = 3.5 \times 10^{-6}$ (abundances given relative to total H). This model is sampled at $r=63$ au, the location of the C_2H emission ring.

et al. 2013; Schwarz et al. 2016; Bergin & Williams 2017; Miotello et al. 2017, 2023). The other is the strong emission from C_2H which rivals that of ^{13}CO (Kastner et al. 2014; Bergin et al. 2016; Miotello et al. 2019) and has been attributed to a C/O ratio that exceeds unity. In the latter case, we cannot rule out a source term for the excess CO in TW Hya from the photoablation of refractory carbon grains as discussed by Bosman et al. (2021a). However, the detection of enriched ^{13}CO within an exoplanetary atmosphere (Zhang et al. 2021) requires a source term for the enrichment. That source term is apparently not carbon isotopic fractionation in the cold interstellar medium based on initial results of ice abundances from JWST (McClure et al. 2023).

In this initial exploration, the evolution of an early-stage disk exposed to cosmic ray ionization offers a potential avenue to generate a ^{13}C enrichment for CO. It simultaneously provides a source term for gas phase hydrocarbons in evolved disk systems whose chemical formation pathways can potentially be powered by photodesorption of hydrocarbon ices. Bosman et al. (2021a) shows that if this carbon is released into the gas via pho-

to-desorption, it can generate a long-lived photochemical equilibrium cycle.

5.1. Disk Ionization

The central need to generate the carbon isotopic fractionation points to the presence of an ionization source deep in the disk. To reach significant mass this source of ionization likely needs the penetrating power of interstellar cosmic rays (Eistrup et al. 2017; Schwarz et al. 2018; Bosman et al. 2018). Based on an analogy to the Sun, and detailed models of cosmic ray-stellar wind interactions it is thought that the interstellar cosmic rays responsible for ionization of H_2 are not present within disk systems that have dissipated their natal envelopes (e.g., class II systems; Cleeves et al. 2013; Fujii & Kimura 2022). Analysis of the observed molecular ion chemistry in class II systems also appear to support reduced interstellar cosmic ray ionization rates (Cleeves et al. 2015; Aikawa et al. 2021; Seifert et al. 2021).

However, the timescales of the CO abundance evolution in disk systems suggest a shift between the protostellar phase, where the envelope is present (e.g., Class 0 and I), and the protoplanetary disk phase (Zhang et al. 2020; Bergner et al. 2020). Thus, chemical processing

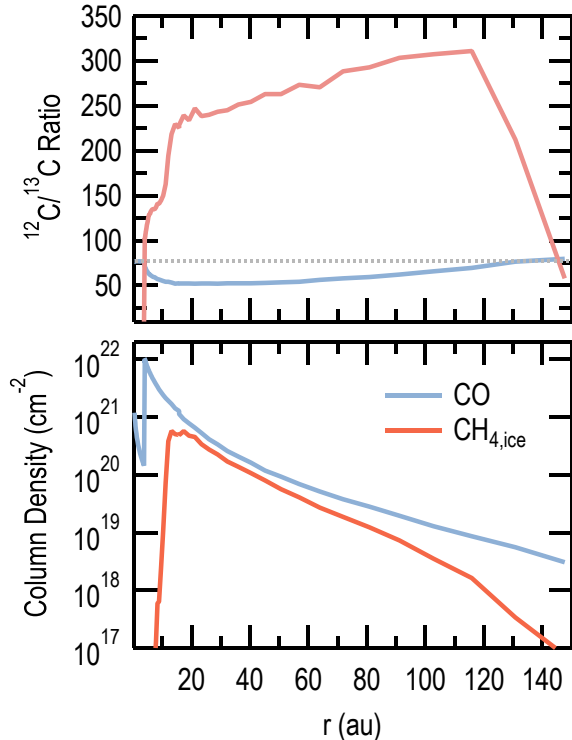


Figure 8. (top) predicted $^{12}\text{CO}/^{13}\text{CO}$ in CO and CH_4 ice as a function of radius from the early-stage disk model. Isotopic ratios are derived through the ratio of the total column densities of the respective isotopologue. (bottom) Predicted total column density profiles for gas phase ^{12}CO and solid state CH_4 as a function of radius for both molecules. Inside ~ 12 au the CH_4 iceline is reached in the midplane and other more complex hydrocarbons with assumed higher sublimation temperatures (e.g. HCCH_2) are created. The drop in the gas phase CO abundance near 4 au is due to an assumed inner dust cavity.

might occur via ionization during earlier evolutionary phases. Indeed, numerous combined observational efforts, over much larger spatial scales, suggest that particle ionization rates might be quite high ($>10^{-15} \text{ s}^{-1}$) during some portion of the protostellar phase (Ceccarelli et al. 2014; Favre et al. 2018; Cabedo et al. 2023; Lattanzi et al. 2023). This is supported by theoretical work that suggest cosmic rays could be generated via shocks within the jets (Padovani et al. 2016; Gaches & Offner 2018). It is worth noting that these observations are obtained on a spatial scale much larger than the young disk. Evidence for enhanced ionization rates is not universal as van’t Hoff et al. (2022) measures a cosmic ray ionization rate below the ISM value in the L1527 protostellar disk. However, if ionization rates are elevated, even for a short timescale, then chemical processing of CO within infalling material or in the protostellar disk

might provide the needed ionization to generate multiple isotopic reservoirs.

5.2. Caveats and the Link to Planets

From the perspective of planet formation and the detected ^{13}C enrichment in an exoplanet by Zhang et al. (2021), the combination of this work and Yoshida et al. (2022a) characterizes the carbon isotopic ratios within the main carbon reservoirs in gas with $\text{C}/\text{O} > 1$. In this gas the ^{13}C carrier is gas-phase CO. If the early-stage disk composition persists to later stages, as observed in TW Hya today, then perhaps gas phase carbon provides the ^{13}C enrichment and not pebbles. One complication is that our early-stage disk model places the ^{13}C deficit as ice coatings of small grains in the upper layers ($z = 5\text{-}15$ au). The evolution of these grains somehow must be separated from CO via dust evolution. Since CO carries the opposite isotopic signature if both reservoirs were available, they would effectively cancel out the enrichment when supplied to a planet. How this might occur is uncertain and more detailed models of coupled gas/grain evolution are needed.

Our models also do not fully match observations. The level of ^{13}CO enrichment in our early-stage disk model (assuming no additional) evolution is only $^{12}\text{CO}/^{13}\text{CO} = 50$ and not the observed level of 20 (Yoshida et al. 2022a). Further, the level of ^{12}C enrichment ($^{12}\text{C}/^{13}\text{C} \sim 250$) in hydrocarbon ices, if they are source terms for C_2H in later stages, is a factor of 3 or more above the carbon isotopic ratio inferred from C_2H via the detection of ^{13}CCH presented here. Our models suggest that, in the context of an assumed low cosmic ray ionization rate, little CO fractionation occurs in the dense disk. Thus, over time the active chemistry in surface layers, perhaps with weak turbulent mixing, would tend to lower the $^{12}\text{C}/^{13}\text{C}$ ratio in C_2H towards the value found for CO. Thus, time evolution could be an answer for C_2H . For CO the higher levels of ^{13}C enrichment would require a different model that is colder and/or with higher ionization rates than the early-stage model adopted here. Regardless the detection of two isotopic reservoirs in carbon (Yoshida et al. 2022a) and nitrogen (Hily-Blant et al. 2019) is providing information on the overall evolution of disk gas.

5.3. Ionization Evolution: Model Predictions

This work highlights the importance of sources of ionization in the dense portion of the disk. Our late-stage model, which matches other aspects of the TW Hya disk (Trapman et al. 2017; Bosman & Banzatti 2019), assumes that the cosmic ray flux impinging on the disk is reduced based on detailed analyses of molecular ion

emission in the TW Hya disk (Cleeves et al. 2015). Under that assumption this model cannot create two disparate carbon isotopic reservoirs. In our work we highlight the potential for ionization evolution as a possible solution to some aspects of this conundrum. This does lead to some testable predictions. If the methane (or hydrocarbon-rich) ice created via CO chemical processing is the source term for the excess carbon that powers C_2H formation, then that ice is predicted to have an extreme carbon isotopic ratio. Further, protostellar disks would have higher levels of methane/hydrocarbon ice (relative to CO ice) when compared to interstellar ices. If this ^{13}C poor material (with $^{12}\text{CH}_{4,ice}/^{13}\text{CH}_{4,ice} \sim 150\text{--}300$) is the source term for today's TW Hya isotopic reservoir then some mixing, as discussed above, is required to lower the isotopic ratio.

Another possibility is that the destruction of refractory carbon powers the formation of C_2H as suggested by Bosman et al. (2021a). In the solar system, refractory carbon carries little carbon isotopic enrichment and is consistent with the interstellar medium (Nomura et al. 2023). This source term would be consistent with our late-stage model for C_2H , but this model cannot fractionate CO. In this case detailed models will be needed to explore how the isotopic signature of this carbon would mix with that of CO to match observations.

6. SUMMARY

We present the first detection of ^{13}CCH in the TW Hya protoplanetary disk system and a detailed analysis of carbon isotopic fractionation in disk systems. Our primary results are as follows.

1. We determine an isotopic ratio for C_2H of $\text{CCH}/^{13}\text{CCH} = 65 \pm 20$ in gas sampling the same radii where Yoshida et al. (2022a) find $\text{CO}/^{13}\text{CO} = 21 \pm 5$. As C_2H is posited as the primary tracer of excess carbon in disks with $\text{C}/\text{O} \geq 1$, this confirms a carbon isotopic dichotomy in this system as suggested by Yoshida et al. (2022a). This is comparable to a similar result found for nitrogen by Hily-Blant et al. (2019).
2. We explore the origins of the carbon isotopic dichotomy through the use an extant thermochemical model of the disk (Trapman et al. 2017; Bosman & Banzatti 2019) with a full model of carbon isotope chemistry (Miotello et al. 2014) in a disk with $\text{C}/\text{O} > 1$ with a reduced carbon content as consistent with observational constraints (Bergin et al. 2016; Kama et al. 2016a; Bosman & Banzatti 2019; Yoshida et al. 2022b). We find that this model is incapable of reproducing two

independent reservoirs primarily due to the lack of cosmic ray ionization in deep disk layers where the temperature would be low enough to power the primary gas phase carbon isotopic fractionation reaction. Additional efforts are needed to model the system adopting all available constraints on both the gas temperature (Calahan et al. 2021) and ionization (Cleeves et al. 2015) simultaneously with the isotopic fractionation.

3. We also explore a model of the TW Hya disk in an earlier evolutionary state where the initial C/O ratio is unity, interstellar cosmic rays are present, and there is no carbon depletion. We find that this model can create two independent isotopic reservoirs one ^{12}C -rich carried by methane and other hydrocarbon ices and the other ^{13}C -rich carried by gas phase carbon monoxide. This dichotomy is predicted to be present throughout the disk and may lay the seeds for the future chemical evolution of the disk as CH_4 is a potential source term for the strong C_2H emission in disk systems (Bosman et al. 2021a).
4. We discuss the implications of this result for exoplanetary systems where gas phase CO appears to be the carrier of ^{13}C enrichments. Additional observational constraints regarding the carbon isotopic ratio within both Class I and Class II disks are sorely needed. Further, an understanding of the ionization evolution of disk systems is critical.

We are grateful to the thorough referee who provided comments that improved this contribution. E.A.B. acknowledges support from NSF grant No. 1907653 and NASA NASA's Emerging Worlds Program, grant 80NSSC20K0333, and Exoplanets Research Program, grant 80NSSC20K0259. KW's research was conducted at the Jet Propulsion Laboratory, California Institute of Technology under contract with the National Aeronautics and Space Administration. KW was supported by a grant from NASA/Emerging Worlds program (18-EW182-0083). L.I.C. acknowledges support from NASA ATP 80NSSC20K0529, the David and Lucille Packard Foundation, and the Research Corporation for Scientific Advancement Cottrell Scholar Award.

This paper makes use of the following ALMA data: ADS/JAO.ALMA#2013.1.00198.S, ADS/JAO.ALMA#2015.1.00308.S.

ALMA is a partnership of ESO (representing its member states), NSF (USA) and NINS (Japan), together with NRC (Canada), MOST and ASIAA (Taiwan), and

KASI (Republic of Korea), in cooperation with the Republic of Chile. The Joint ALMA Observatory is operated by ESO, AUI/NRAO and NAOJ. The National

Radio Astronomy Observatory is a facility of the National Science Foundation operated under cooperative agreement by Associated Universities, Inc.

REFERENCES

- Aikawa, Y., Miyama, S. M., Nakano, T., & Umebayashi, T. 1996, *ApJ*, 467, 684
- Aikawa, Y., van Zadelhoff, G. J., van Dishoeck, E. F., & Herbst, E. 2002, *A&A*, 386, 622
- Aikawa, Y., Cataldi, G., Yamato, Y., et al. 2021, *ApJS*, 257, 13
- Andrews, S. M., Wilner, D. J., Zhu, Z., et al. 2016, *ApJ*, in press.
- Arce, H. G., Shepherd, D., Gueth, F., et al. 2007, in *Protostars and Planets V*, ed. B. Reipurth, D. Jewitt, & K. Keil, 245
- Barman, T. S., Konopacky, Q. M., Macintosh, B., & Marois, C. 2015, *ApJ*, 804, 61
- Bergin, E. A., Cleeves, L. I., Crockett, N., & Blake, G. A. 2014, *Faraday Discuss.*, 168, 61.
<http://dx.doi.org/10.1039/C4FD00003J>
- Bergin, E. A., Du, F., Cleeves, L. I., et al. 2016, *ApJ*, 831, 101
- Bergin, E. A., & Williams, J. P. 2017, *Formation, Evolution, and Dynamics of Young Solar Systems*, 445, in press
- Bergner, J. B., Öberg, K. I., Bergin, E. A., et al. 2020, *ApJ*, 898, 97
- Bosman, A. D., Alarcón, F., Zhang, K., & Bergin, E. A. 2021a, *ApJ*, 910, 3
- Bosman, A. D., & Banzatti, A. 2019, *A&A*, 632, L10
- Bosman, A. D., Walsh, C., & van Dishoeck, E. F. 2018, *A&A*, 618, A182
- Bosman, A. D., Bergin, E. A., Loomis, R. A., et al. 2021b, *ApJS*, 257, 15
- Broggi, M., & Birkby, J. 2021, in *ExoFrontiers; Big Questions in Exoplanetary Science*, ed. N. Madhusudhan, 8–1
- Bruderer, S. 2013, *A&A*, 559, A46
- Bruderer, S., van Dishoeck, E. F., Doty, S. D., & Herczeg, G. J. 2012, *A&A*, 541, A91
- Cabedo, V., Maury, A., Girart, J. M., et al. 2023, *A&A*, 669, A90
- Calahan, J. K., Bergin, E., Zhang, K., et al. 2021, *ApJ*, 908, 8
- Ceccarelli, C., Caselli, P., Bockelée-Morvan, D., et al. 2014, *Protostars and Planets VI*, 859
- Cleeves, L. I., Adams, F. C., & Bergin, E. A. 2013, *ApJ*, 772, 5
- Cleeves, L. I., Bergin, E. A., Qi, C., Adams, F. C., & Öberg, K. I. 2015, *ApJ*, 799, 204
- Cleeves, L. I., Öberg, K. I., Wilner, D. J., et al. 2018, *ApJ*, 865, 155
- Cridland, A. J., Pudritz, R. E., & Birnstiel, T. 2016, *MNRAS*, submitted
- Czekala, I., Loomis, R. A., Teague, R., et al. 2021, *ApJS*, 257, 2
- Du, F., Bergin, E. A., & Hogerheijde, M. R. 2015, *ApJL*, 807, L32
- Du, F., Bergin, E. A., Hogerheijde, M., et al. 2017, *ApJ*, 842, 98
- Eistrup, C., Walsh, C., & van Dishoeck, E. F. 2017, *A&A*, in press
- Favre, C., Cleeves, L. I., Bergin, E. A., Qi, C., & Blake, G. A. 2013, *ApJL*, 776, L38
- Favre, C., Ceccarelli, C., López-Sepulcre, A., et al. 2018, *ApJ*, 859, 136
- Fujii, Y. I., & Kimura, S. S. 2022, *ApJL*, 937, L37
- Furuya, K., & Aikawa, Y. 2014, *ApJ*, 790, 97
- Furuya, K., Aikawa, Y., Sakai, N., & Yamamoto, S. 2011, *ApJ*, 731, 38
- Gaches, B. A. L., & Offner, S. S. R. 2018, *ApJ*, 861, 87
- Guillot, T., Fletcher, L. N., Helled, R., et al. 2023, in *Astronomical Society of the Pacific Conference Series*, Vol. 534, *Protostars and Planets VII*, ed. S. Inutsuka, Y. Aikawa, T. Muto, K. Tomida, & M. Tamura, 947
- Helled, R., & Guillot, T. 2017, in *Handbook of Exoplanets*
- Hily-Blant, P., Magalhaes de Souza, V., Kastner, J., & Forveille, T. 2019, *A&A*, 632, L12
- Hsieh, C.-H., Arce, H. G., Li, Z.-Y., et al. 2023, *ApJ*, 947, 25
- Huang, J., Andrews, S. M., Dullemond, C. P., et al. 2018, *ApJL*, 869, L42
- Igea, J., & Glassgold, A. E. 1999, *ApJ*, 518, 848
- JWST Transiting Exoplanet Community Early Release Science Team, Ahrer, E.-M., Alderson, L., et al. 2023, *Nature*, 614, 649
- Kama, M., Bruderer, S., van Dishoeck, E. F., et al. 2016a, *A&A*, in press.
- Kama, M., Bruderer, S., Carney, M., et al. 2016b, *A&A*, in press
- Kastner, J. H., Hily-Blant, P., Rodriguez, D. R., Punzi, K., & Forveille, T. 2014, *ApJ*, 793, 55

- Krijt, S., Bosman, A. D., Zhang, K., et al. 2020, *ApJ*, 899, 134
- Krijt, S., Ciesla, F. J., & Bergin, E. A. 2016, *ApJ*, in press
- Langer, W. D., & Graedel, T. E. 1989, *ApJS*, 69, 241
- Langer, W. D., Graedel, T. E., Frerking, M. A., & Armentrout, P. B. 1984, *ApJ*, 277, 581
- Langer, W. D., & Penzias, A. A. 1993, *ApJ*, 408, 539
- Lattanzi, V., Alves, F. O., Padovani, M., et al. 2023, *A&A*, 671, A35
- Lavie, B., Mendonça, J. M., Mordasini, C., et al. 2017, *AJ*, 154, 91
- Line, M. R., Brogi, M., Bean, J. L., et al. 2021, *Nature*, 598, 580
- Maret, S., & Bergin, E. A. 2007, *ApJ*, 664, 956
- McClure, M. K., Rocha, W. R. M., Pontoppidan, K. M., et al. 2023, *Nature Astronomy*, 7, 431
- Milam, S. N., Savage, C., Brewster, M. A., Ziurys, L. M., & Wyckoff, S. 2005, *ApJ*, 634, 1126
- Minissale, M., Aikawa, Y., Bergin, E., et al. 2022, *ACS Earth and Space Chemistry*, 6, 597
- Miotello, A., Bruderer, S., & van Dishoeck, E. F. 2014, *A&A*, 572, A96
- Miotello, A., Kamp, I., Birnstiel, T., Cleeves, L. C., & Kataoka, A. 2023, in *Astronomical Society of the Pacific Conference Series*, Vol. 534, *Protostars and Planets VII*, ed. S. Inutsuka, Y. Aikawa, T. Muto, K. Tomida, & M. Tamura, 501
- Miotello, A., van Dishoeck, E. F., Williams, J. P., et al. 2017, *A&A*, 599, A113
- Miotello, A., Facchini, S., van Dishoeck, E. F., et al. 2019, *A&A*, 631, A69
- Nomura, H., Furuya, K., Cordiner, M. A., et al. 2023, in *Astronomical Society of the Pacific Conference Series*, Vol. 534, *Protostars and Planets VII*, ed. S. Inutsuka, Y. Aikawa, T. Muto, K. Tomida, & M. Tamura, 1075
- Öberg, K. I., Boogert, A. C. A., Pontoppidan, K. M., et al. 2011a, *ApJ*, 740, 109
- Öberg, K. I., Murray-Clay, R., & Bergin, E. A. 2011b, *ApJL*, 743, L16
- Öberg, K. I., Guzmán, V. V., Walsh, C., et al. 2021, *ApJS*, 257, 1
- Oreshenko, M., Lavie, B., Grimm, S. L., et al. 2017, *ApJL*, 847, L3
- Padovani, M., Marcowith, A., Hennebelle, P., & Ferrière, K. 2016, *A&A*, 590, A8
- Reboussin, L., Wakelam, V., Guilloteau, S., Hersant, F., & Dutrey, A. 2015, *A&A*, 579, A82
- Redaelli, E., Sipilä, O., Padovani, M., et al. 2021, *A&A*, 656, A109
- Röllig, M., & Ossenkopf, V. 2013, *A&A*, 550, A56
- Roueff, E., Loison, J. C., & Hickson, K. M. 2015, *A&A*, 576, A99
- Schwarz, K. R., Bergin, E. A., Cleeves, L. I., et al. 2016, *ApJ*, 823, 91
- . 2018, *ApJ*, 856, 85
- Seifert, R. A., Cleeves, L. I., Adams, F. C., & Li, Z.-Y. 2021, *ApJ*, 912, 136
- Sokal, K. R., Deen, C. P., Mace, G. N., et al. 2018, *ApJ*, 853, 120
- Stelzer, B., & Schmitt, J. H. M. M. 2004, *A&A*, 418, 687
- Teague, R. 2019, *The Journal of Open Source Software*, 4, 1632
- Teague, R., Bae, J., & Bergin, E. A. 2019, *Nature*, 574, 378–381
- Trapman, L., Miotello, A., Kama, M., van Dishoeck, E. F., & Bruderer, S. 2017, *A&A*, 605, A69
- van Boekel, R., Henning, T., Menu, J., et al. 2017, *ApJ*, 837, 132
- van't Hoff, M. L. R., Leemker, M., Tobin, J. J., et al. 2022, *ApJ*, 932, 6
- Visser, R., van Dishoeck, E. F., & Black, J. H. 2009, *A&A*, 503, 323
- Woods, P. M., & Willacy, K. 2009, *ApJ*, 693, 1360
- Yen, H.-W., Koch, P. M., Liu, H. B., et al. 2016, *ApJ*, 832, 204
- Yoshida, T. C., Nomura, H., Furuya, K., Tsukagoshi, T., & Lee, S. 2022a, *ApJ*, 932, 126
- Yoshida, T. C., Nomura, H., Tsukagoshi, T., Furuya, K., & Ueda, T. 2022b, *ApJL*, 937, L14
- Yoshida, T. C., Nomura, H., Furuya, K., et al. 2024, *arXiv e-prints*, arXiv:2403.00626
- Zhang, K., Bergin, E. A., Blake, G. A., Cleeves, L. I., & Schwarz, K. R. 2017, *Nature Astronomy*, 1, 0130
- Zhang, K., Bergin, E. A., Schwarz, K., Krijt, S., & Ciesla, F. 2019, *ApJ*, 883, 98
- Zhang, K., Schwarz, K. R., & Bergin, E. A. 2020, *ApJL*, 891, L17
- Zhang, Y., Snellen, I. A. G., Bohn, A. J., et al. 2021, *Nature*, 595, 370

APPENDIX

A. DALI MODEL FOR TW HYA

This model is based on the code and parameters as published by [Trapman et al. \(2017\)](#) and modified by [Bosman & Banzatti \(2019\)](#). We adopt this model as a baseline and change a few parameters to investigate the chemical evolution at a slightly earlier evolutionary stage.

Table 3. TW Hya Model Parameters^a

Stellar parameters	
Stellar mass	0.74 M_{\odot}
Stellar luminosity	1 L_{\odot}
X-ray luminosity	10^{30} erg s ⁻¹
UV Luminosity	2.7×10^{31} erg s ⁻¹
Disk parameters	
Disk mass	0.025 M_{\odot}
Critical radius (R_c)	35 AU
Surface density slope (γ)	1
scale-height at R_c (h_c)	0.1 rad
Flaring angle (ψ)	0.3
Inner radius	0.05 AU
Gap inner radius	0.3 AU
Gap outer radius	2.4 AU
Inner disk gas-to-dust	100
Inner disk gas depletion	10^{-2}
Small dust size	0.005–1 μm
Small dust fraction	0.01 (late-stage), 0.10 (early-stage)
Large dust size	0.005–1000 μm
Large dust fraction	0.99 (late-stage), 0.90 (early-stage)
Large dust settling factor	0.2
Cosmic Ray Ionization Rate	10^{-19} s ⁻¹ (late-stage), 5×10^{-17} s ⁻¹ (early-stage)

^a [Trapman et al. \(2017\)](#); [Bosman & Banzatti \(2019\)](#)